Available online at www.sciencedirect.com
SCIENCE DIRECT®
Journal of Computational Physics 203 (2005) 405–421
JOURNAL OF COMPUTATIONAL PHYSICS
www.elsevier.com/locate/jcp

# A multidimensional gas-kinetic BGK scheme for hypersonic viscous flow

Kun Xu [a,*], Meiliang Mao [b], Lei Tang [c]

[a] *Department of Mathematics, Hong Kong University of Science and Technology, Clear Water Bay, Kowloon, Hong Kong, China*
[b] *China Aerodynamics Research and Development Center, Sichuan, China*
[c] *ZONA Technology Inc., Scottsdale, AZ 85251, USA*

Received 13 May 2004; received in revised form 6 September 2004; accepted 6 September 2004
Available online 12 October 2004

## Abstract

This paper concerns the development and application of a gas-kinetic scheme based on the Bhatnagar–Gross–Krook (BGK) model for the Navier–Stokes equations in the study of hypersonic viscous flow. Firstly, we extend the gas-kinetic Navier–Stokes solver [K. Xu, A gas-kinetic BGK scheme for the Navier–Stokes equations and its connection with artificial dissipation and Godunov method, J. Comput. Phys. 171 (2001) 289–335] by implementing a multidimensional particle propagation mechanism in the flux evaluation, where the gradients of flow variables in both normal and tangential directions of a cell interface are explicitly included. With the construction of a time averaged flux function, an implicit BGK scheme with LU-SGS method is constructed. The main purpose of the current research is to pave the way to extend the current approach directly to the flow computation with unstructured mesh, where the flow gradients in both parallel and perpendicular directions around a cell interface can be explicitly taken into account in a viscous flow computation. In the numerical parts, we concentrate on the computation of heat flux in laminar hypersonic viscous flows, where complicated flow phenomena, i.e., shock boundary layer interaction, flow separation, and viscous/inviscid interaction, will be encountered. The cases studied include the type IV shock–shock interaction around a circular cylinder and hypersonic flow passing through a double-cone geometry. In the hypersonic viscous flow, in comparison with the capturing of velocity and pressure fields, the accurate computation of stress and heat flux bears large difficulties. In all cases studied here, the heat fluxes obtained across body surfaces have good agreement with the experimental measurements.

*MSC:* 65M06; 76P05; 76T05
*Keywords:* Navier–Stokes equations; Gas-kinetic scheme; Hypersonic flow; Heat flux

---

[*] Corresponding author. Tel.: +852 2358 7433; fax: +852 2358 1643.
*E-mail address:* makxu@ust.hk (K. Xu).

0021-9991/$ - see front matter © 2004 Elsevier Inc. All rights reserved.
doi:10.1016/j.jcp.2004.09.001

## 1. Introduction

An important issue in the design and development of aerospace vehicles is the effect of various types of flow phenomena on aerodynamic performance and aerothermal loads. Evaluation of aerodynamic heating during reentry flight is one of the key issues. To the current stage, the computation of the interaction between a shock wave and a separated region in the hypersonic flow is still a very challenging problem in computational fluid dynamics. In terms of heat transfer, significant differences between the computational results and experiments indicate that further investigation and design of more accurate viscous flow solvers are needed to understand these phenomena. The severe heating rates produced by the viscous/inviscid interactions and by the shock/shock interactions can cause catastrophic failure for the vehicles in the hypersonic flight. Over the past 15 years there have been concerted efforts both in Europe and America to validate the Navier–Stokes and DSMC-based methods in the description of complex hypersonic flows. Extensive codes validation have been conducted. A number of experiments specifically designed with simple model configuration in the laminar hypervelocity flow have been constructed and continuously being used to examine complex flow phenomena, such as the viscous/inviscid interactions. For example, the double cone geometry case [8], which is also calculated in this paper, is one of the standard cases for the validation of the Navier–Stokes solvers. Due to the sensitivity of the size of separation zone induced by the interaction between the viscous boundary layer and the shock wave on the numerical dissipation, it becomes a good case for testing the Navier–Stokes codes. Also, the type IV shock wave interactions around a circular cylinder, with a view to simulating the pressure and heating rate augmentation caused by an impinging shock on the leading edge of a cowl lip of an engine inlet, bears great arguments about the steady or unsteady nature due to its complicated flow structure and delicate sensitivity of the solution on numerical schemes. As shown in this paper a steady state solution is obtained by the current scheme for the type IV shock interaction case.

It is well known that based on the gas-kinetic theory, the Navier–Stokes equations can be derived from the Boltzmann equation using the Chapman–Enskog expansion. Therefore, a Navier–Stokes solver can be equally constructed by solving the Boltzmann equation, even with a simplified collision model [3,2]. In the gas-kinetic representation, all flow variables become the moments of a single particle distribution function. Since a gas distribution function is used to describe both equilibrium and non-equilibrium states, the inviscid and viscous fluxes are obtained simultaneously in the gas-kinetic scheme. However, in the traditional upwinding schemes for the Navier–Stokes solutions, an operator splitting method is commonly adopted, where the Riemann solver or equivalent flux evaluation based on two constant states is used for the inviscid part and the central differences for the viscous and heat conduction parts. Theoretically, the use of different flow distributions for the inviscid and viscous parts is artificial, which may introduce numerical error in the cases with strong coupling between the inviscid and viscous interactions. For example, the dissipative characteristic of upwind schemes in the regions with sharp gradients, such as in the boundary layer, may trigger unsteady mechanism to prevent it from obtaining steady state solution. Even though high-order discretizations can be introduced for the inviscid and viscous parts separately, an operator splitting error due to the different initial condition (or equivalently kinematic dissipation) can be hardly eliminated, especially in the cases with severe coupling between transport and dissipative heating. This may have a determinant consequence on the prediction of heat transfer rates [13], and on the results of the flows which are sensitive to the numerical dissipation, such as the type IV shock–shock interaction case. On the contrary, for the gas-kinetic BGK scheme, both inviscid and viscous parts are recovered in a single gas distribution function $f$. The time evolution of $f$ is based on the same initial condition. As pointed out earlier [25], the gas-kinetic description is capable of giving a more complete description of the non-equilibrium flow. Even though the non-equilibrium parts in a gas-distribution function have no direct contribution to the macroscopic mass, momentum and energy densities, they do contribute to the higher moments, such as the fluxes. The current kinetic scheme is based on the collisional gas-kinetic BGK model. In the conventional approach, the collisionless Boltzmann equation is employed to derive the formula for the numerical flux. The theory of kinetic equation for the numerical flux has been studied recently by Ohwada [15,16], and the role of collision effect is clarified there. Based on Ohwada's railroad theory, the current gas-kinetic BGK scheme can be proved to have second accuracy for the Navier–Stokes equations.

In this paper, we are going to first introduce a multidimensional gas-kinetic BGK scheme, where the gradients of flow variables in both normal and tangential directions around a cell interface are accounted in the flux evaluation. Then the scheme is applied to the study of laminar hypersonic viscous flows. The cases studied include flow passing a cylinder, type IV shock–shock interactions, and $M = 8.03$ flow impinging on a double-cone geometry. In these cases, complicated flow structures, such as shock–shock, shock–boundary interactions, as well as separated flow regions, are all encountered. All these cases are very sensitive to the dissipation in a numerical scheme which could directly effect the size of the separated region and the intensity of heat transport.

## 2. A multidimensional BGK scheme

Similar to the MUSCL type approach, the first step for the gas kinetic BGK scheme is to interpolate the macroscopic flow variables inside each computational cell. In order to keep the integrity of the gas-kinetic scheme, as most previous approaches the van Leer limiter is used for the initial data reconstruction of conservative variables [19]. The fundamental task in the construction of a finite-volume gas-kinetic scheme is to evaluate a time-dependent gas distribution function $f$ at a cell interface, from which the numerical flux can be obtained. Instead of using the slopes in the normal direction only at a cell interface, the slopes in the tangential direction are also included in the current method. Denote $x = 0$, $y \in [-\Delta y/2, \Delta y/2]$ as a cell interface, on both sides of this interface the interpolated macroscopic variables have gradients $(\nabla\rho, \nabla(\rho U), \nabla(\rho V), \nabla E)$, where $\rho$, $\rho U$, $\rho V$, and $E$ are the densities of mass, momentum, and energy. The above gradients are not necessarily in the normal direction of the cell interface.

The BGK model can be written as [1]:

$$f_t + uf_x + vf_y = \frac{g - f}{\tau}, \tag{1}$$

where $f$ is the gas distribution function and $g$ is the equilibrium state approached by $f$. Both $f$ and $g$ are functions of space $(x, y)$, time $t$, particle velocities $(u, v)$, and internal variable $\xi$. The particle collision time $\tau$ is related to the viscosity and heat conduction coefficients. The equilibrium state is a Maxwellian distribution,

$$g = \rho\left(\frac{\lambda}{\pi}\right)^{\frac{K+2}{2}} \mathrm{e}^{-\lambda((u-U)^2+(v-V)^2+\xi^2)},$$

where $\rho$ is the density, $U$ and $V$ are the macroscopic velocities in the $x$ and $y$-directions, and $\lambda$ is related to the gas temperature, i.e., $m/2kT$. For a 2D flow, the particle motion in the $z$-direction is included into the internal variable $\xi$, and the total number of degrees of freedom $K$ in $\xi$ is equal to $(5 - 3\gamma)/(\gamma - 1) + 1$. For example, for a diatomic gas, $K$ is equal to 3 to account for the random motion in the $z$-direction and two rotational internal degree of freedom. In the equilibrium state, $\xi^2$ is equal to $\xi^2 = \xi_1^2 + \xi_2^2 + \cdots + \xi_K^2$. The underlying assumption in the above equilibrium state is that each degree of freedom shares the same amount of internal energy $kT/2$, or the so-called equilibrium flow. The effect of the internal degree of freedom on the viscous stress, such as the bulk viscosity, will be introduced at the end of this section.

The relation between mass $\rho$, momentum $(n = \rho U, m = \rho V)$, and energy $E$ densities with the distribution function $f$ is

$$w = \begin{pmatrix} \rho \\ n \\ m \\ E \end{pmatrix} = \int \psi_\alpha f \, \mathrm{d}\Xi, \quad \alpha = 1\text{–}4, \tag{2}$$

where $\psi_\alpha$ is the component of the vector of moments

$$\boldsymbol{\psi} = (\psi_1, \psi_2, \psi_3, \psi_4)^{\mathrm{T}} = \left(1, u, v, \tfrac{1}{2}(u^2 + v^2 + \xi^2)\right)^{\mathrm{T}},$$

and $\mathrm{d}\Xi = \mathrm{d}u \, \mathrm{d}v \, \mathrm{d}\xi$ is the volume element in the phase space with $\mathrm{d}\xi = \mathrm{d}\xi_1 \, \mathrm{d}\xi_2 \cdots \mathrm{d}\xi_K$. Since mass, momentum and energy are conserved during particle collisions, $f$ and $g$ satisfy the conservation constraint

$$\int (g - f)\psi_\alpha \, \mathrm{d}\Xi = 0, \quad \alpha = 1\text{–}4, \tag{3}$$

at any point in space and time. The derivation from the BGK model to the NS equations can be found in [20,24].

The general solution $f$ of the BGK model at a cell interface $(x_{i+1/2}, y_j)$ and time $t$ is

$$f(x_{i+1/2}, y_j, t, u, v, \xi) = \frac{1}{\tau} \int_0^t g(x', y', t', u, v, \xi) \mathrm{e}^{-(t-t')/\tau} \, \mathrm{d}t' + \mathrm{e}^{-t/\tau} f_0(x_{i+1/2} - ut, y_j - vt), \tag{4}$$

where $x' = x_{i+1/2} - u(t - t')$, $y' = y_j - v(t - t')$ are the trajectory of a particle motion and $f_0$ is the initial gas distribution function $f$ at the beginning of each time step ($t = 0$). Two unknowns $g$ and $f_0$ must be specified in Eq. (4) in order to obtain the solution $f$. In order to simplify the notation, ($x_{i+1/2} = 0$, $y_j = 0$) will be used in the following text.

Based on the Chapman–Enskog expansion of the BGK model (1), the gas distribution function up to the Navier–Stokes order at the point ($x = 0$, $y = 0$) and time ($t = 0$) has the form [17],

$$f_{\mathrm{NS}} = g - \tau(g_t + ug_x + vg_y),$$

where $\phi_1 = -\tau(g_t + ug_x + vg_y)$ has to satisfy the compatibility condition $\int \psi_\alpha \phi_1 \, \mathrm{d}\Xi = 0$. To the 2nd-order accuracy, the gas distribution around the point ($x = 0$, $y = 0$) at time $t = 0$ can be approximated as

$$f_{\mathrm{NS}} = g + g_x x + g_y y - \tau(g_t + ug_x + vg_y).$$

Therefore, in the multidimensional gas-kinetic scheme with the initial discontinuous macroscopic variables at the left and right hand sides of a cell interface the initial gas distribution function $f_0$ has the form,

$$f_0 = \begin{cases} g^{\mathrm{l}}(1 + a^{\mathrm{l}}x + b^{\mathrm{l}}y - \tau(a^{\mathrm{l}}u + b^{\mathrm{l}}v + A^{\mathrm{l}})), & x \leqslant 0, \\ g^{\mathrm{r}}(1 + a^{\mathrm{r}}x + b^{\mathrm{r}}y - \tau(a^{\mathrm{r}}u + b^{\mathrm{r}}v + A^{\mathrm{r}})), & x \geqslant 0, \end{cases} \tag{5}$$

where $g^{\mathrm{l}}a^{\mathrm{l}}$, $g^{\mathrm{r}}a^{\mathrm{r}}$, $g^{\mathrm{l}}A^{\mathrm{l}}$ and $g^{\mathrm{r}}A^{\mathrm{r}}$ are related to the spatial and temporal derivatives of the equilibrium states. Here, different from directional splitting method, $g^{\mathrm{l}}b^{\mathrm{l}}$ and $g^{\mathrm{r}}b^{\mathrm{r}}$ correspond to the gradients in the tangential direction along the cell interface. Here the terms proportional to $\tau$ represent the non-equilibrium parts in the Chapman–Enskog expansion. Note that the non-equilibrium parts have no direct contribution to the conservative flow variables, i.e.,

$$\begin{aligned} &\int (a^{\mathrm{l}}u + b^{\mathrm{l}}v + A^{\mathrm{l}})\psi_\alpha g^{\mathrm{l}} \, \mathrm{d}\Xi = 0, \\ &\int (a^{\mathrm{r}}u + b^{\mathrm{r}}v + A^{\mathrm{r}})\psi_\alpha g^{\mathrm{l}} \, \mathrm{d}\Xi = 0, \end{aligned} \tag{6}$$

which are the exact equations to determine $A^{\mathrm{l}}$ and $A^{\mathrm{r}}$. In the above $f_0$, $g^{\mathrm{l}}$, $g^{\mathrm{r}}$, $a^{\mathrm{l}}$, and $a^{\mathrm{r}}$ have the same definition as the corresponding parameters in the BGK-NS method [25].

After having $f_0$, the equilibrium state $g$ around ($x = 0$, $y = 0$, $t = 0$) is constructed as

$$g = g_0\big(1 + (1 - H[x])\bar{a}^{\mathrm{l}}x + H[x]\bar{a}^{\mathrm{r}}x + \bar{b}y + \bar{A}t\big), \tag{7}$$

where $\bar{b}$ is the additional term related to the flow variations in the tangential direction, and $H[x]$ is the Heaviside function defined as

$$H[x] = \begin{cases} 0, & x < 0, \\ 1, & x \geqslant 0. \end{cases}$$

Here $g_0$ is a local Maxwellian distribution function located at ($x = 0$, $y = 0$). In both $f_0$ and $g$, $a^{\mathrm{l}}$, $A^{\mathrm{l}}$, $a^{\mathrm{r}}$, $A^{\mathrm{r}}$, $\bar{a}^{\mathrm{l}}$, $\bar{a}^{\mathrm{r}}$, $\bar{b}$, and $\bar{A}$ are related to the derivatives of a Maxwellian in space and time.

The dependences of $a^{\mathrm{l}}, a^{\mathrm{r}}, \ldots, \bar{A}$ on the particle velocities can be obtained from a Taylor expansion of a Maxwellian and have the following form,

$$\begin{aligned}
a^{\mathrm{l}} &= a^{\mathrm{l}}_1 + a^{\mathrm{l}}_2 u + a^{\mathrm{l}}_3 v + a^{\mathrm{l}}_4 \tfrac{1}{2}(u^2 + v^2 + \xi^2) = a^{\mathrm{l}}_\alpha \psi_\alpha, \\
A^{\mathrm{l}} &= A^{\mathrm{l}}_1 + A^{\mathrm{l}}_2 u + A^{\mathrm{l}}_3 v + A^{\mathrm{l}}_4 \tfrac{1}{2}(u^2 + v^2 + \xi^2) = A^{\mathrm{l}}_\alpha \psi_\alpha, \\
&\cdots \\
\bar{A} &= \bar{A}_1 + \bar{A}_2 u + \bar{A}_3 v + \bar{A}_4 \tfrac{1}{2}(u^2 + \xi^2) = \bar{A}_\alpha \psi_\alpha,
\end{aligned}$$

where $\alpha = 1$–$4$ and all coefficients $a^{\mathrm{l}}_1, a^{\mathrm{l}}_2, \ldots, \bar{A}_4$ are local constants.

With the initial data reconstruction, we have obtained the distributions $\bar{\rho}_j(x,y)$, $\bar{m}_j(x,y)$, $\bar{n}_j(x,y)$, and $\bar{E}_j(x,y)$ inside each cell. At the center of a cell interface ($x_{i+1/2}$, $y_j$), the left and right macroscopic states are

$$\bar{w}_i(x_{i+1/2}, y_j) = \begin{pmatrix} \bar{\rho}_i(x_{i+1/2}, y_j) \\ \bar{m}_i(x_{i+1/2}, y_j) \\ \bar{n}_i(x_{i+1/2}, y_j) \\ \bar{E}_i(x_{i+1/2}, y_j) \end{pmatrix}; \qquad \bar{w}_{i+1}(x_{i+1/2}, y_j) = \begin{pmatrix} \bar{\rho}_{i+1}(x_{i+1/2}, y_j) \\ \bar{m}_{i+1}(x_{i+1/2}, y_j) \\ \bar{n}_{i+1}(x_{i+1/2}, y_j) \\ \bar{E}_{i+1}(x_{i+1/2}, y_j) \end{pmatrix}.$$

By using the relation between the gas distribution function $f$ and the macroscopic variables (Eq. (2)), we get

$$\int g^{\mathrm{l}}\psi_\alpha \,\mathrm{d}\Xi = \bar{w}_i(x_{i+1/2}, y_j); \qquad \int g^{\mathrm{l}}a^{\mathrm{l}}\psi_\alpha \,\mathrm{d}\Xi = \vec{n} \cdot \nabla w^{\mathrm{l}}, \tag{8}$$

$$\int g^{\mathrm{r}}\psi_\alpha \,\mathrm{d}\Xi = \bar{w}_{i+1}(x_{i+1/2}, y_j); \qquad \int g^{\mathrm{r}}a^{\mathrm{r}}\psi_\alpha \,\mathrm{d}\Xi = \vec{n} \cdot \nabla w^{\mathrm{r}}, \tag{9}$$

where $\nabla w^{\mathrm{l}}$ and $\nabla w^{\mathrm{r}}$ are the gradients of macroscopic variables on the left and right hand sides of a cell interface, and $\vec{n}$ is the unit normal direction. With the definition of Maxwellian distributions

$$g^{\mathrm{l}} = \rho^{\mathrm{l}}\left(\frac{\lambda^{\mathrm{l}}}{\pi}\right)^{\frac{K+2}{2}} \mathrm{e}^{-\lambda^{\mathrm{l}}((u-U^{\mathrm{l}})^2 + (v-V^{\mathrm{l}})^2 + \xi^2)}$$

and

$$g^{\mathrm{r}} = \rho^{\mathrm{r}}\left(\frac{\lambda^{\mathrm{r}}}{\pi}\right)^{\frac{K+2}{2}} \mathrm{e}^{-\lambda^{\mathrm{r}}((u-U^{\mathrm{r}})^2 + (v-V^{\mathrm{r}})^2 + \xi^2)},$$

and from Eqs. (8) and (9), the parameters in $g^{\mathrm{l}}$, $g^{\mathrm{r}}$, $a^{\mathrm{l}}$, and $a^{\mathrm{r}}$ can be uniquely determined. The detailed formulation can be found in [25]. Similarly, in the tangential direction $b^{\mathrm{l}}$ and $b^{\mathrm{r}}$ can be obtained from

$$\int g^{\mathrm{l}} b^{\mathrm{l}} \psi_\alpha \, \mathrm{d}\Xi = \vec{t} \cdot \nabla w^{\mathrm{l}}; \qquad \int g^{\mathrm{r}} b^{\mathrm{r}} \psi_\alpha \, \mathrm{d}\Xi = \vec{t} \cdot \nabla w^{\mathrm{r}},$$

where $\vec{t}$ is the unit vector in the tangential direction along the cell interface.

After determining the terms $a^{\mathrm{l}}$, $b^{\mathrm{l}}$, $a^{\mathrm{r}}$, and $b^{\mathrm{r}}$, $A^{\mathrm{l}}$ and $A^{\mathrm{r}}$ in $f_0$ can be found from Eq. (6), which are

$$\begin{aligned} M^{\mathrm{l}}_{\alpha\beta} A^{\mathrm{l}}_\beta &= -\frac{1}{\rho^{\mathrm{l}}} \int (a^{\mathrm{l}} u + b^{\mathrm{l}} v) \psi_\alpha \, \mathrm{d}\Xi, \\ M^{\mathrm{r}}_{\alpha\beta} A^{\mathrm{r}}_\beta &= -\frac{1}{\rho^{\mathrm{r}}} \int (a^{\mathrm{r}} u + b^{\mathrm{r}} v) \psi_\alpha \, \mathrm{d}\Xi, \end{aligned} \tag{10}$$

where $M^{\mathrm{r}}_{\alpha\beta} = \int g^{\mathrm{r}} \psi_\alpha \psi_\beta \, \mathrm{d}\Xi / \rho^{\mathrm{r}}$. Again, $M_{\alpha\beta}$ have the same definition as the directional splitting BGK-NS method [25].

For the equilibrium state $g$ in Eq. (7), the corresponding values of $\rho_0$, $U_0$, $V_0$ and $\lambda_0$ in $g_0$,

$$g_0 = \rho_0 \left(\frac{\lambda_0}{\pi}\right)^{\frac{K+2}{2}} \mathrm{e}^{-\lambda_0((u-U_0)^2 + (v-V_0)^2 + \xi^2)},$$

can be found as follows. Taking the limit $t \to 0$ in Eq. (4) and substituting its solution into Eq. (3), the conservation constraint at ($x_{i+1/2}$, $y_j$, $t = 0$) gives

$$\int g_0 \psi_\alpha \, \mathrm{d}\Xi = w_0 = \int_{u>0} \int g^{\mathrm{l}} \psi_\alpha \, \mathrm{d}\Xi + \int_{u<0} \int g^{\mathrm{r}} \psi_\alpha \, \mathrm{d}\Xi, \tag{11}$$

where $w_0 = (\rho_0, m_0, n_0, E_0)^{\mathrm{T}}$. Since $g^{\mathrm{l}}$ and $g^{\mathrm{r}}$ have been obtained earlier, the above moments can be evaluated explicitly. Therefore, the conservative variables $\rho_0$, $m_0$, $n_0$, and $E_0$ at the cell interface can be evaluated, from which $g_0$ is uniquely determined. For example, $\lambda_0$ in $g_0$ can be found from

$$\lambda_0 = (K+2)\rho_0 / (4(E_0 - \tfrac{1}{2}(m_0^2 + n_0^2)/\rho_0)).$$

Then, $\bar{a}^{\mathrm{l}}$ and $\bar{a}^{\mathrm{r}}$ of $g$ in Eq. (7) can be obtained through the relation of

$$\frac{\bar{w}_{i+1}(x_{i+1}, y_j) - w_0}{\rho_0 \Delta x^+} = \bar{M}^0_{\alpha\beta} \begin{pmatrix} \bar{a}^{\mathrm{r}}_1 \\ \bar{a}^{\mathrm{r}}_2 \\ \bar{a}^{\mathrm{r}}_3 \\ \bar{a}^{\mathrm{r}}_4 \end{pmatrix} = \bar{M}^0_{\alpha\beta} \bar{a}^{\mathrm{r}}_\beta \tag{12}$$

and

$$\frac{w_0 - \bar{w}_i(x_i, y_j)}{\rho_0 \Delta x^-} = \bar{M}^0_{\alpha\beta} \begin{pmatrix} \bar{a}^{\mathrm{l}}_1 \\ \bar{a}^{\mathrm{l}}_2 \\ \bar{a}^{\mathrm{l}}_3 \\ \bar{a}^{\mathrm{l}}_4 \end{pmatrix} = \bar{M}^0_{\alpha\beta} \bar{a}^{\mathrm{l}}_\beta, \tag{13}$$

where $\Delta x^- = x_{i+1/2} - x_i$ and $\Delta x^+ = x_{i+1} - x_{i+1/2}$ are the distances from the cell interface to cell centers. Since the matrix $\bar{M}^0_{\alpha\beta} = \int g_0 \psi_\alpha \psi_\beta \, \mathrm{d}\Xi / \rho_0$ is known, $(\bar{a}^{\mathrm{r}}_1, \bar{a}^{\mathrm{r}}_2, \bar{a}^{\mathrm{r}}_3, \bar{a}^{\mathrm{r}}_4)^{\mathrm{T}}$ and $(\bar{a}^{\mathrm{l}}_1, \bar{a}^{\mathrm{l}}_2, \bar{a}^{\mathrm{l}}_3, \bar{a}^{\mathrm{l}}_4)^{\mathrm{T}}$ can be evaluated accordingly. The term $\bar{b}$ is evaluated from

$$\int \bar{b} \psi \, \mathrm{d}\Xi = \int_{u>0} b^{\mathrm{l}} \psi \, \mathrm{d}\Xi + \int_{u<0} b^{\mathrm{r}} \psi \, \mathrm{d}\Xi. \tag{14}$$

Up to this point, we have determined all parameters in the initial gas distribution function $f_0$ and the equilibrium state $g$ at the beginning of each time step $t = 0$. After substituting Eqs. (5) and (7) into Eq. (4), the gas distribution function $f$ at a cell interface can be expressed as

$$\begin{aligned} f(x_{i+1/2}, y_j, t, u, v, \xi) = {} & (1 - \mathrm{e}^{-t/\tau})g_0 + \left(\tau(-1 + \mathrm{e}^{-t/\tau}) + t\,\mathrm{e}^{-t/\tau}\right)\left(\bar{a}^{\mathrm{l}} H[u] + \bar{a}^{\mathrm{r}}(1 - H[u]) + \bar{b}v\right)ug_0 \\ & + \tau(t/\tau - 1 + \mathrm{e}^{-t/\tau})\bar{A}g_0 + \mathrm{e}^{-t/\tau}\left((1 - (t + \tau)(ua^{\mathrm{l}} + vb^{\mathrm{l}}))H[u]g^{\mathrm{l}}\right. \\ & \left. + (1 - (t + \tau)(ua^{\mathrm{r}} + vb^{\mathrm{r}}))(1 - H[u])g^{\mathrm{r}}\right) + \mathrm{e}^{-t/\tau}\left(-\tau A^{\mathrm{l}} H[u]g^{\mathrm{l}} - \tau A^{\mathrm{r}}(1 - H[u])g^{\mathrm{r}}\right). \end{aligned} \tag{15}$$

The only unknown left in the above expression is $\bar{A}$. Since both $f$ (Eq. (15)) and $g$ (Eq. (7)) contain $\bar{A}$, the integration of the conservation constraint (Eq. (3)) at $x_{i+1/2}$, $y_j$ over the whole time step $\Delta t$ gives

$$\int_0^{\Delta t} \int (g - f)\psi_\alpha \,\mathrm{d}t\,\mathrm{d}\Xi = 0,$$

which can be used to get $\bar{A}$ uniquely. The above gas-kinetic method is similar to that in [25], except additional terms $b^{\mathrm{l}}$, $b^{\mathrm{r}}$, and $\bar{b}$ terms related to the flow variations in the tangential direction are included in the current method.

Finally, the time-dependent numerical fluxes in the normal-direction across the cell interface can be computed by

$$\begin{pmatrix} \mathscr{F}_\rho \\ \mathscr{F}_m \\ \mathscr{F}_n \\ \mathscr{F}_E \end{pmatrix}_{i+1/2} = \int u \begin{pmatrix} 1 \\ u \\ v \\ \frac{1}{2}(u^2 + v^2 + \xi^2) \end{pmatrix} f(x_{i+1/2}, y_j, t, u, v, \xi)\mathrm{d}\Xi, \tag{16}$$

where $f(x_{i+1/2}, y_j, t, u, v, \xi)$ is given by Eq. (15). In order to develop an implicit gas-kinetic BGK solver, a time averaged flux function is needed. For example, based on the above flux function for a cell $(i, j)$ we first calculate the time averaged residual in that cell,

$$R_{i,j} = \frac{1}{\Delta t}\int_0^{\Delta t}\left(\frac{\mathscr{F}_{i+1/2,j} - \mathscr{F}_{i-1/2,j}}{\Delta x} + \frac{\mathscr{G}_{i,j+1/2} - \mathscr{G}_{i,j-1/2}}{\Delta y}\right)\mathrm{d}t,$$

where $\mathscr{F}$ and $\mathscr{G}$ are the numerical fluxes equation (16) around the four interfaces of the cell $(i, j)$. With the above residual, an implicit gas-kinetic BGK code using the LU-SGS technique [28] can be written as

$$\left(D_x^- A^+ + D_x^+ A^- + D_y^- B^+ + D_y^+ B^-\right)\Delta W = -R,$$

where $R$ is the residual vector and $\Delta W = W_{i,j}^{n+1} - W_{i,j}^n$. The flux Jacobian denoted by $A = \partial F/\partial W$ and $B = \partial G/\partial W$ are evaluated based on the Euler fluxes and the splitting of $A$ and $B$ have the form

$$A^\pm = R_A \Lambda_A^\pm L_A, \qquad B^\pm = R_B \Lambda_B^\pm L_B.$$

Here $L_A$, $L_B$, $R_A$ and $R_B$ are the left and right eigenvector of $A$ and $B$. In the LU-SGS formulation, the splitting of Matrix $\Lambda^\pm$ is given by

$$\Lambda^\pm = \tfrac{1}{2}(\Lambda \pm rI),$$

where $I$ is an identity matrix and $r$ is the corresponding largest eigenvalue in matrix $A$ and $B$.

With the above gas-kinetic flux function, the viscous flow with unit Prandtl number is basically simulated. In order to study the flow with any realistic Prandtl number, a Prandtl number fix based on the modification of energy flux can be used [25]. In all simulations for the air flow in the next section, the Prandtl number is equal to 0.72. The collision time $\tau$ is determined by $\tau = \mu/p$, and the Sutherland's law is used for the viscosity coefficient,

$$\mu = \mu_\infty \left(\frac{T}{T_\infty}\right)^{3/2} \frac{T_\infty + S}{T + S},$$

where $T_\infty = 285$ K and $S = 110.4$ K. Theoretically, for a diatomic gas with the assumption of equi-partition for each degree of freedom, the above BGK scheme is solving the NS equations with both dynamic and bulk viscosities. The viscous stress of the kinetic scheme has the form [24],

$$\sigma_{kl} = \tau p\left[\left(\frac{\partial U_k}{\partial x_l} + \frac{\partial U_l}{\partial x_k} - \frac{2}{3}\delta_{kl}\frac{\partial U_i}{\partial x_i}\right) + \frac{2\mathscr{K}}{3(\mathscr{K}+3)}\delta_{kl}\frac{\partial U_i}{\partial x_i}\right],$$

where $\mathscr{K}$ accounts for the two rotational degree of freedom. Therefore, for all air flow cases in the next section we are solving Navier–Stokes equations with both the first and second viscosity coefficients $\mu = \tau p$ and $\eta = 4/15\mu$. In the evaluation of the heat flux across the boundary of flying objects, we first obtain the temperature gradient in the normal direction $\partial T/\partial n$ along the wall, then the Fourier's law is used to get the heat flux $\mathbf{q} = -\kappa \partial T/\partial n$, where the heat conduction coefficient is obtained based on the viscosity coefficient and the Prandtl number $Pr$, i.e., $\kappa = C_p\mu/Pr$.

## 3. The study of hypersonic viscous flows

Evaluation of aerodynamic heating during re-entry flight is one of the key issues in the design of vehicle. However, typical viscous hypersonic flows about bodies display steep gradients not only in regions

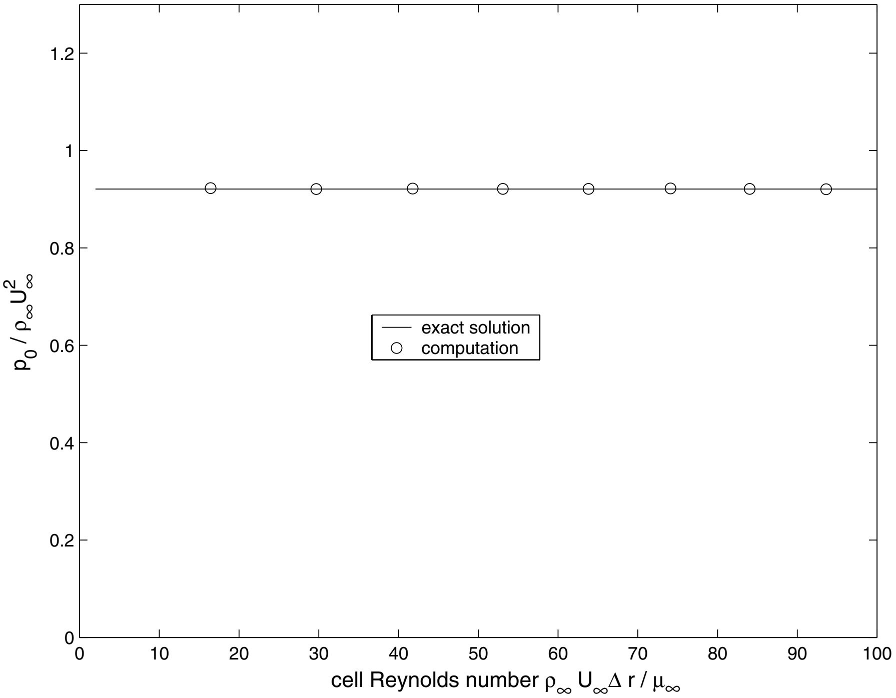

Fig. 1. Calculated stagnation pressure vs. cell Reynolds number.

with shocks but also in the boundary layers. It is still a great challenge for the accurate computation of hypersonic viscous flow by the current CFD methods, especially for the accurate capturing of heat flow. In this section, we are going to concentrate on the calculation of the heat flow in the cases where complicated flow structures, such as shock–shock, shock–boundary layer, as well as separated flows, are involved. In all following calculations, the non-slip isothermal boundary condition is used along body surfaces.

**Case 1.** (Hypersonic flow passing through a circular cylinder) This case is taken from the experiment done by Wieting [21], where the inflow condition for the air is

$$M_\infty = 8.03, \quad T_\infty = 124.94\ \mathrm{K}, \quad T_\mathrm{w} = 294.44\ \mathrm{K}, \quad Re = 1.835 \times 10^5.$$

The computational mesh used in this study is $35 \times 63$. In our calculations, due to different mesh construction the cell Reynolds number is defined in the current paper by

$$Re_\mathrm{cell} = \rho_\infty U_\infty \Delta r / \mu_\infty,$$

where $\Delta r$ is the mesh size of the first cell in the normal direction next to the cylinder surface, which varies from 1 to 100. Note some authors use the definition $R_\mathrm{cell} = (\rho c \Delta r/\mu)_\mathrm{wall}$ as the cell Reynolds number, where $c$ is the sound speed. The calculated stagnation pressure $p/(\rho_\infty U_\infty^2)$ with the change of cell Reynolds number $Re_\mathrm{cell}$ is shown in Fig. 1, and the heat flux $q/(\rho_\infty U_\infty^3)$ at the stagnation point is shown in Fig. 2. The exact solutions in both figures are the grid converged solution at the stagnation point, where the pressure has the value 0.9209 and the heat flux is equal to 0.003655. Fig. 3 shows the normalized pressure and heat flux at the cylindrical surface, where both experiments and computation results are included. The computed

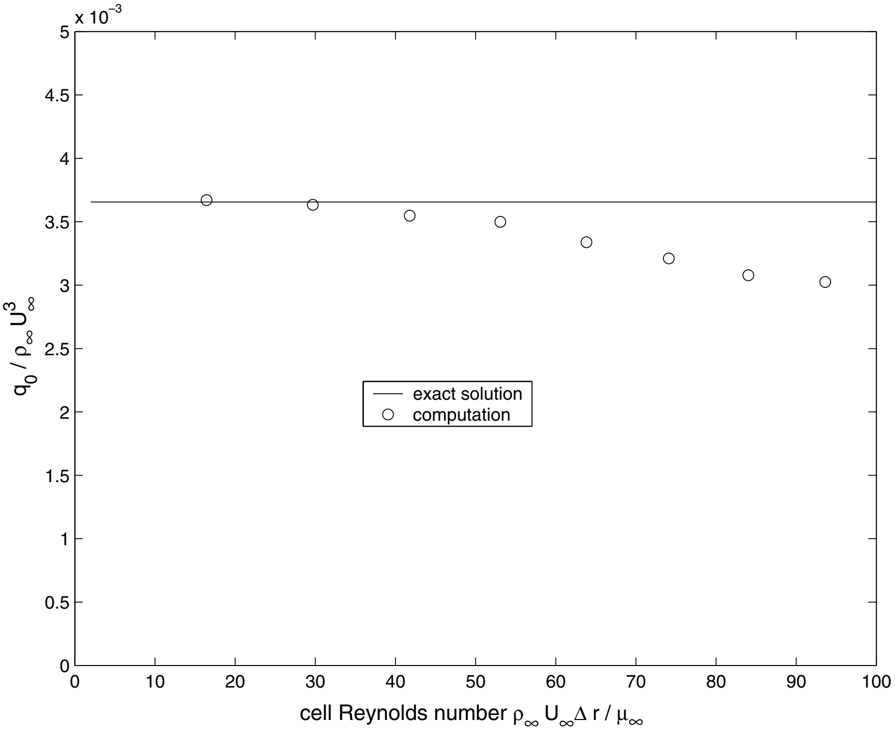

Fig. 2. Calculated stagnation point heat flux vs. cell Reynolds number.

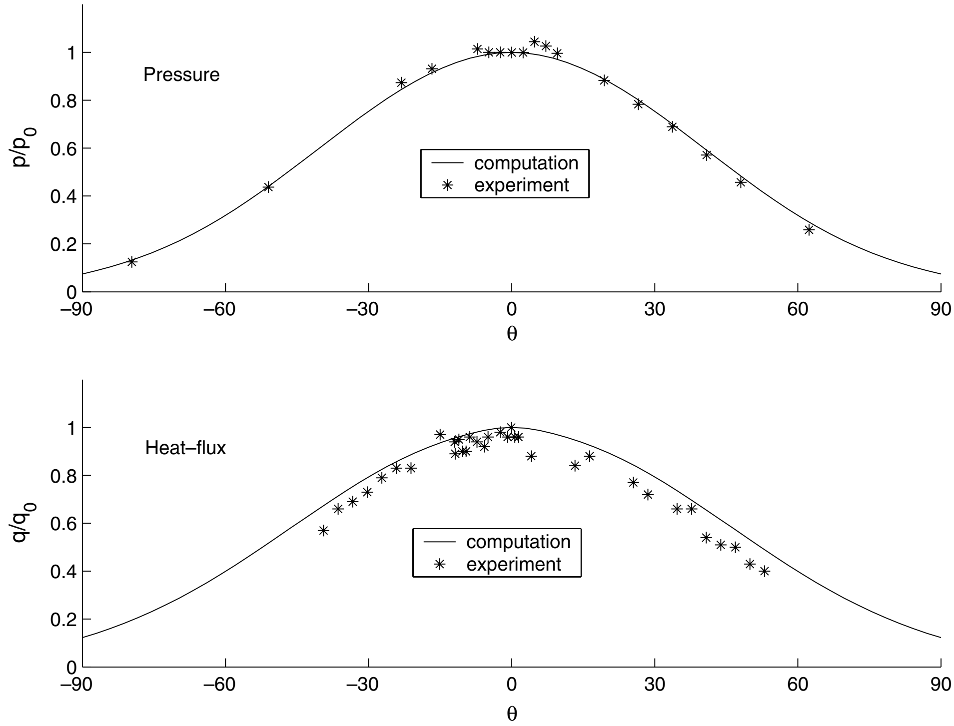

Fig. 3. Pressure (upper) and heat flux (lower) along the cylindrical surface, where the symbols are the experimental data [21] and the solid lines are the computational results.

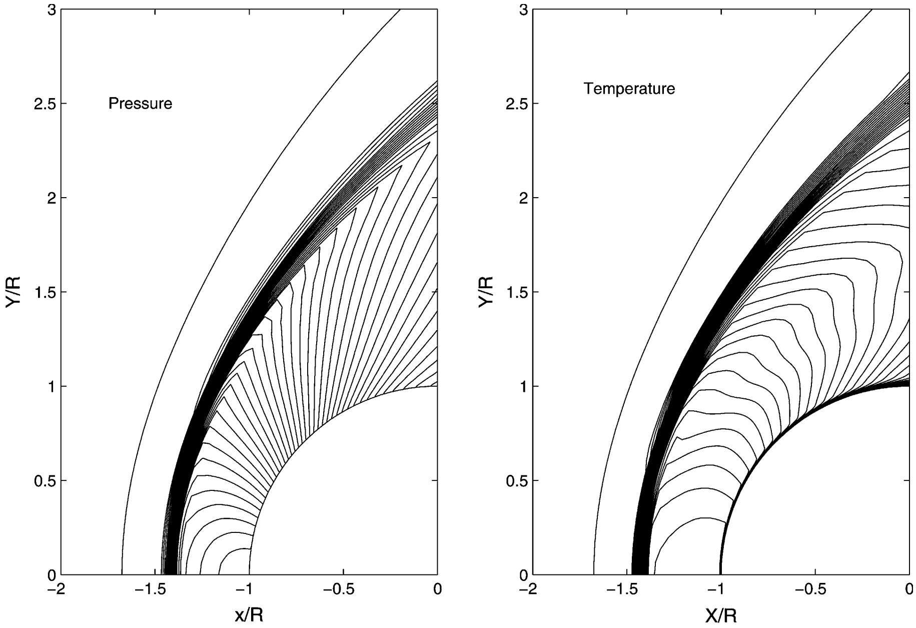

Fig. 4. Pressure and temperature contours.

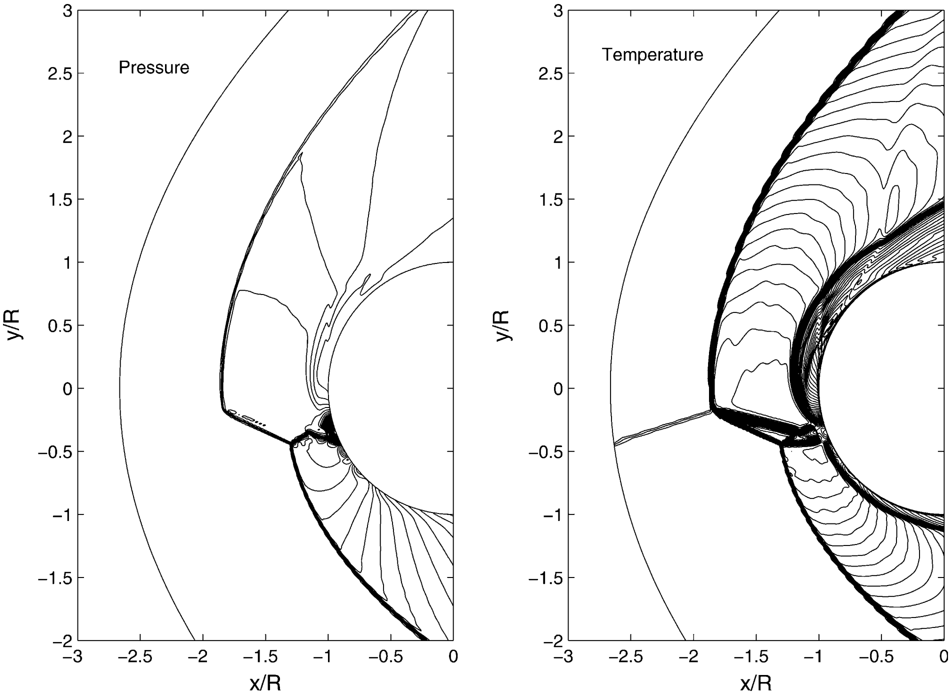

Fig. 5. Pressure and temperature distribution of type IV shock–shock interaction.

pressure and temperature contours around the cylinders are shown in Fig. 4. From this case, we can realize that the BGK scheme can basically capture the pressure and heat flux.

**Case 2.** (Type IV shock–shock interaction around a circular cylinder) Shock/shock interaction was classified by Edney [5] into six patterns, which depend on the impinging position and angle. It results in a very complex flow field with high pressure and heat flux peak in localized region. Of special interest in this investigation is the type IV interaction, which occurs when the incident shock impinges on the bow shock in a

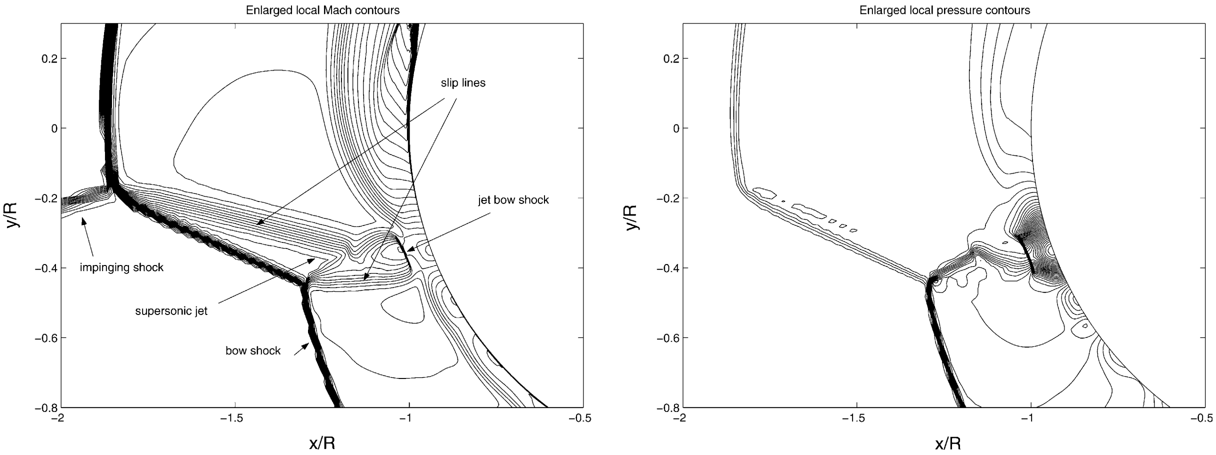

Fig. 6. Local Mach and pressure contours in the supersonic jet region.

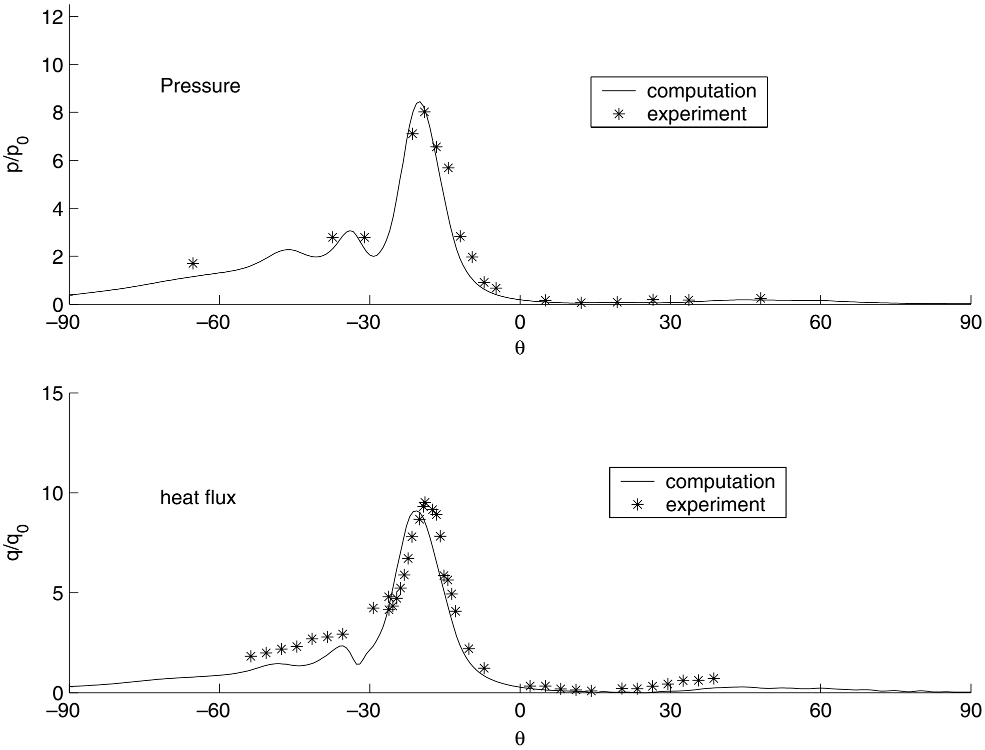

Fig. 7. Pressure (upper) and heat flux (lower) along the cylindrical surface, where the symbols are the experimental data [21] and the solid lines are the computational results.

region where the flow behind it is subsonic. The type IV interaction is the most severe case to form the hot spot on the surface of the cylinder due to the supersonic jet hitting on the wall. The interaction results in the formation of a supersonic impinging jet, a series of shock waves, expansion waves, and shear layers in a local area of interaction. The supersonic impinging jet, which is bounded by two shear layers separating the jet from the upper and lower subsonic regions, impinges on the body surface, and is terminated by a jet bow shock just ahead of the surface. This impinging jet bow shock wave creates a small stagnation region of high temperature, pressure, and heating rates. Meanwhile, shear layers are formed to separate the supersonic jet from the lower and upper subsonic regions.

The experimental data were collected by Wieting and Holden [21,22]. In the past decade, many methods have been used in the study of this case [12,18,6,9,27,29,11,30]. Due to the complicated flow interactions and different numerical approaches used, the steady state solutions have hardly been obtained, even with higher-order accuracy method.

In the current calculation, before imposing the incident oblique shock, the initial condition for the inflow is

$$M_\infty = 8.03, \quad T_\infty = 122.11\ \mathrm{K}, \quad T_\mathrm{w} = 294.44\ \mathrm{K}, \quad Re = 1.94 \times 10^5.$$

Based on the experimental measurement and the numerical calculations, Thareja et al. [18] summarized that the position of incident impinging shock on the cylinder can be approximated by the curve $y = 0.3271x + 0.4147$ for the experiment (Run 21) [21,22], where ($x = 0$, $y = 0$) is the center of the cylinder.

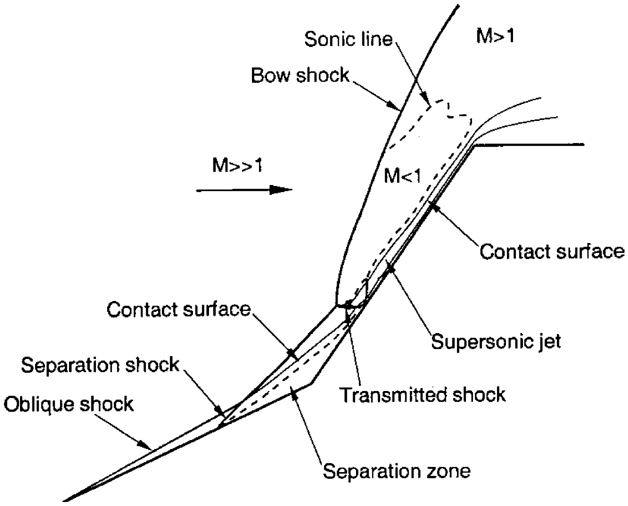

Fig. 8. Schematic flow structure for double-cone geometry [14].

Our simulations are based on 181 × 300 mesh points with a cell Reynolds number $Re_{\text{cell}} = 4.6$. A steady state solution is obtained from the explicit scheme after a long time integration with the iterative steps on the order of $10^7$, where the residual is decreased to the order of $10^{-7}$ and the flow structure keeps the same form. Note that the explicit scheme uses a time step which has the local CFL number on the order of 0.1. The implicit scheme doesn't converge for the type IV shock interaction case. The pressure and

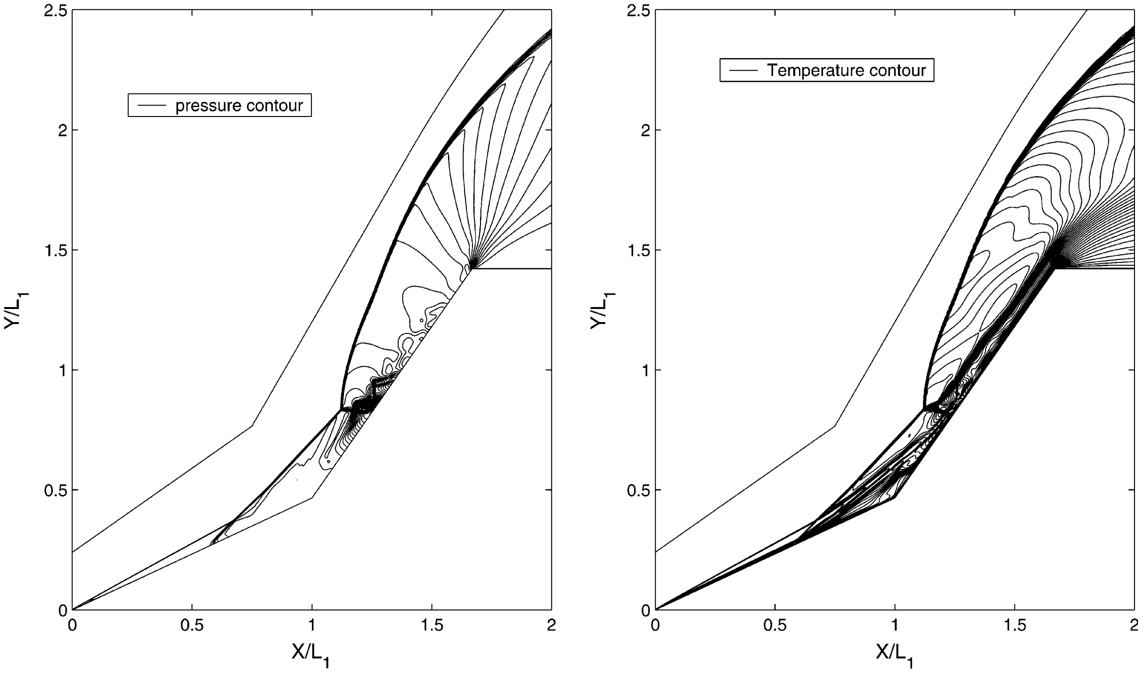

Fig. 9. Pressure and temperature distribution around double cone geometry.

temperature contours around the cylinder are shown in Fig. 5. The flow patterns, i.e., the Mach number and pressure, in the supersonic jet region are shown in Fig. 6. This figure clearly shows the strong jet bow shock and hot spot around the cylindrical surface. The measured as well as computational pressure and heat flux along the cylindrical surface are shown in Fig. 7, where the symbols are the experimental data [21,22] and solid lines are computational results. In comparison with other numerical observations, excellent match between the experimental measurement and computations are obtained. A similar result with 270 × 300 mesh points has also been obtained. Different from the conclusion in [29], a steady state solution is obtained in our calculation, at least under the current flow condition. Indeed, complicated flow structures, such as shear layer, impinging jet, as well as bow shocks, exist in the current case.

**Case 3.** (Axis-symmetric double cone geometry with flow separation) The double-cone configuration has a first cone half-angle 25° and the second cone angle 55°. Under the experimental condition (Run 28) [8], the incident flow has

$$\rho_\infty = 0.6545 \times 10^{-3}\ \mathrm{kg/m^3}, \quad U_\infty = 2664.0\ \mathrm{m/s}, \quad T_\infty = 185.56\ \mathrm{K}, \quad T_{\mathrm{wall}} = 293.33\ \mathrm{K}.$$

The corresponding Mach and Reynolds number are

$$M_\infty = 9.59, \quad Re = 13090.$$

In all series of experiments, the RUN 28 with the above flow condition is the most difficult one to be calculated due to the large flow separation region. Under this flow condition, the first cone produces an attached shock wave, and the second cone with larger angle produces a detached bow shock. These two

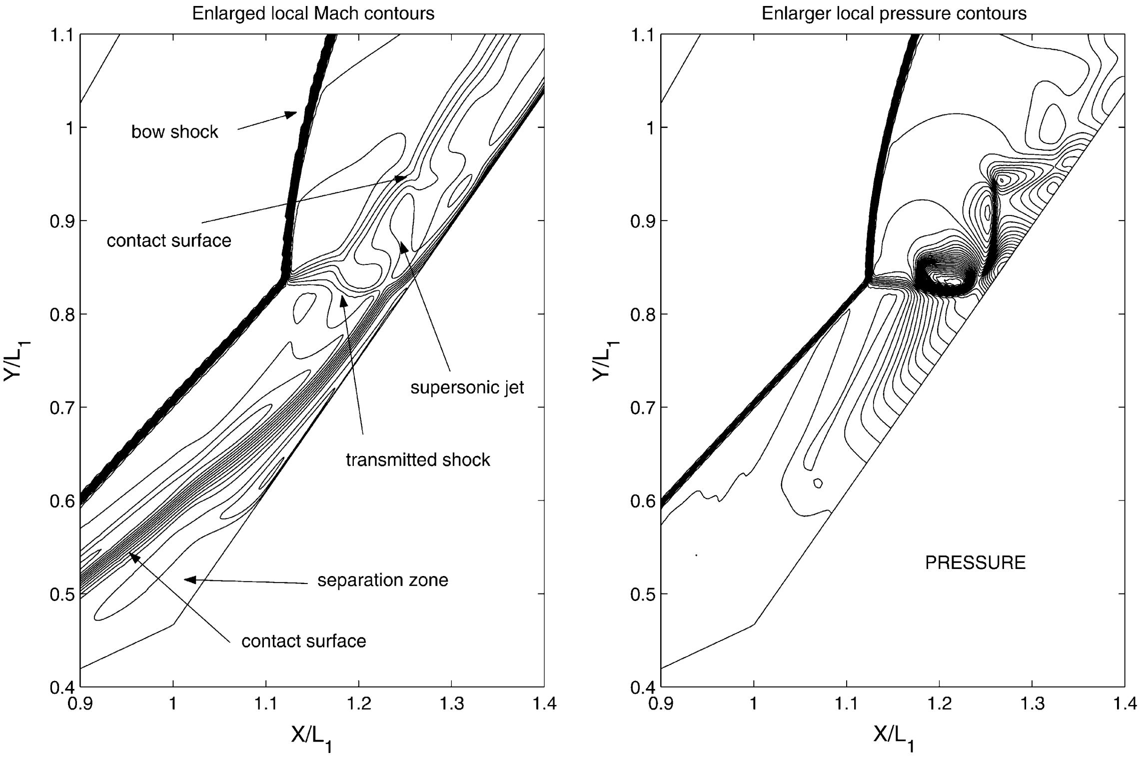

Fig. 10. Enlarged local Mach (left) and pressure (right) contours around the surface of second cone.

shocks interact to form a transmitted shock that strikes the second cone surface near the cone–cone juncture. The adverse pressure gradient due to the cone juncture and the transmitted shock generates a large region of separated flow that produces its own separation shock. This shock interacts with the attached shock from the first cone, altering the interaction with the detached shock from the second cone. This in turn effects the size of the separation region. The shock interaction produces very high surface pressure and heat transfer rates where the transmitted shock impinges on the second cone. As presented in [14], the schematic flow structure is shown in Fig. 8. Many authors have conducted the simulation for this case [7,4,10,23].

The coupling between the shock waves and the separation zone makes this flow very sensitive to the physical modelling of the flow and to the numerical methods. In order to get grid refinement results, we have run this case with the following mesh

$$(250 \times 100, 500 \times 100, 1000 \times 100, 500 \times 200, 1000 \times 200, 1000 \times 400).$$

Basically there is no differences in the flow distributions when using $500 \times 200$ and $1000 \times 400$ grid points. The computed pressure and temperature contours with $500 \times 200$ points are shown in Fig. 9, where the cell Reynolds number on the order 1 is used in the computation. The Mach number and pressure distributions around the second cone surface are shown in Fig. 10, where the contact surfaces, transmitted shock, as well as supersonic shock can be seen clearly. Along the cone surfaces, the measured and computational pressure and heat flux are presented in Fig. 11, where the symbols are the experimental results [8]. As shown in these figures, the size of the separation region and the heat fluxes on the cone surfaces match

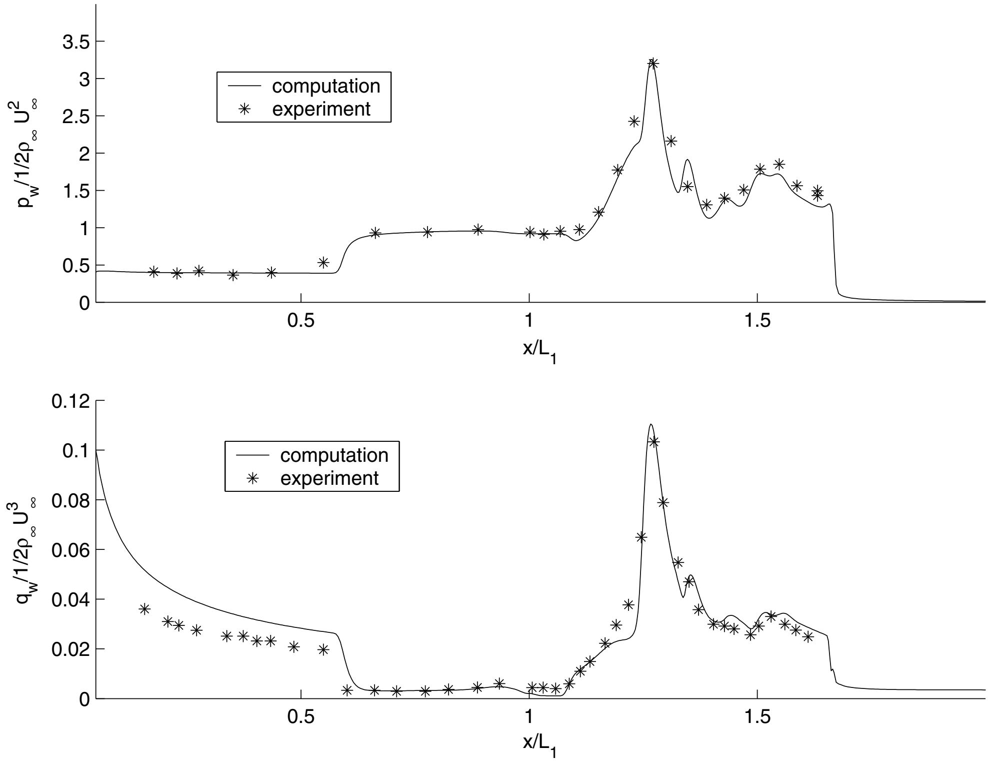

Fig. 11. Pressure (upper) and heat flux (lower) along cone surface, where the symbols are the experimental data [8] and the solid lines are the computational results.

the experimental data excellently. Especially along the surface of the 2nd-cone, the complicated flow structures are captured. As analyzed in [14], the deviation in the heat flux before the separation shock along the first cone surface is due to the non-equilibrium nature in the incoming expansion gas in the experiment device. In our simulation, the ideal equilibrium incoming gas is assumed.

For most test cases in this section, the steady state is obtained based on the LU-SGS technique. In terms of the flux evaluation, the current multidimensional BGK solver takes 30% more computational time than the directional splitting BGK-NS method [25]. However, in terms of the accuracy the differences from the multidimensional and BGK-NS schemes in the heat flux and pressure distributions are marginal. It may be due to the strong shock discontinuities involved in all these test cases, where the large amount of numerical dissipation is introduced in the discontinuous region. For the smooth and continuous low speed flows, the current multidimensional gas-kinetic scheme goes to the kinetic method in [26], which does give much more accurate results than the corresponding directionally splitting method.

## 4. Conclusion

In this paper, we first present a multidimensional gas-kinetic BGK flow solver for the compressible Navier–Stokes equations. Then, this newly developed scheme is applied to the laminar hypersonic viscous flow, where complicated flow structures are involved. For the viscous flow computation, the difference between the gas-kinetic BGK scheme and the traditional upwinding method is that the inviscid and viscous terms are included in a single gas distribution function in the kinetic approach and the time evolution is based on the same initial macroscopic flow distributions. However, for the traditional methods, an operator splitting technique is always used, where the inviscid and viscous terms are discretized based on different flow distributions. The laminar hypersonic viscous flows studied in this paper include the Run 28 of the double cone geometries and the shock–shock interactions. The complicated flow patterns, such as shock–shock, shock boundary layer, and inviscid–viscous interactions, are well captured. For example, a steady state flow structure in type IV shock–shock interaction around a circular cylinder is obtained. The good agreement between the simulation results and the experimental measurements, especially the heat flux around body surfaces, shows clearly that the gas-kinetic scheme is a reliable viscous flow solvers, even though it does not solve the compressible Navier–Stokes equations directly.

## Acknowledgements

The authors would like to thank Prof. G.V. Candler and Dr. I. Nompelis for providing their AIAA papers. This research was supported by Hong Kong Research Grant Council. Additional support was provided by US Air Force Research Laboratory under contract F33615-03-M-3329-C.

## References

[1] P.L. Bhatnagar, E.P. Gross, M. Krook, A model for collision processes in gases i: small amplitude processes in charged and neutral one-component systems, Phys. Rev. 94 (1954) 511–525.
[2] G.A. Bird, Molecular Gas Dynamics and the Direct Simulation of Gas Flows, Oxford Science Publications, Oxford, 1994.
[3] C. Cercignani, Rarefied Gas Dynamics, Cambridge University Press, Cambridge, 2000.
[4] G.V. Candler, I. Nompelis, M.C. Druguet, Navier–Stokes predictions of hypersonic double-cone and cylinder-flare fields, AIAA paper 2001–1024, 39th AIAA Aerospace Sciences Meeting and Exhibit, January 8–11, 2001.
[5] B. Edney, Anomalous heat transfer and pressure distributions on blunt bodies at hypersonic speeds in the presence of an imping shock, FFA Report 115, Aero. Res. Institute of Sweden, 1986.

[6] D.V. Gaitonde, J.S. Shang, The performance of flux-split algorithms in high-speed viscous flows, AIAA paper 92-0186, 1992.

[7] D.V. Gaitonde, P.W. Canupp, Heat transfer prediction in a laminar hypersonic viscous/inviscid interaction, J. Thermophys. Heat Transfer 16 (2002) 481–489.

[8] M.S. Holden, T.P. Wadhams, A review of experimental studies for DSMC and Navier–Stokes code validation in laminar regions of shock/shock and shock boundary layer interaction including real gas effects in hypervelocity flows, AIAA 2003–3641, 2003.

[9] K. Hsu, I.H. Parpia, Simulation of multiple shock–shock interference patterns on a cylindrical leading edge, AIAA J. 34 (1996) 764–771.

[10] P.A. Gnoffo, Computational aerothermodynamics in aeroassist applications, AIAA paper 2001-2632, 2001.

[11] C.E. Glass, Numerical simulation of low-density shock-wave interactions, NASA/TM-1999-209358, 1999.

[12] G.H. Klopfer, H.C. Yee, Viscous hypersonic shock on shock interaction on blunt cowl lips, AIAA paper 88-0233, 1988.

[13] R.W. MacCormack, G.V. Candler, The solution of the Navier–Stokes equations using gauss-seidel line relaxation, Comp. Fluids 17 (1989) 135–150.

[14] I. Nompelis, G.V. Candler, M.S. Holden, Effect of vibrational nonequilibrium on hypersonic double-cone experiments, AIAA J. 41 (2003) 2162–2169.

[15] T. Ohwada, On the construction of kinetic schemes, J. Comput. Phys. 177 (2002) 156–175.

[16] T. Ohwada, S. Kobayashi, Management of the discontinuous reconstruction in kinetic schemes, J. Comput. Phys. 197 (2004) 116–138.

[17] T. Ohwada, K. Xu, The kinetic scheme for the full Burnett equations, J. Comput. Phys., 201 (2004) 315–332.

[18] R.R. Thareja, et al., A point implicit unstructured grid solver for the Euler and Navier–Stokes equations, Int. J. Numer. Methods Fluids 9 (1989) 405–425.

[19] B. van Leer, Toward the ultimate conservative difference scheme iv, a new approach to numerical convection, J. Comput. Phys. 23 (1977) 276–299.

[20] W.G. Vincenti, C.H. Kruger Jr., Introduction to Physical Gas Dynamics, John Wiley and Sons, New York, 1965.

[21] A.R. Wieting, Experimental study of shock wave interface heating on a cylindrical leading edge, NASA TM-100484, 1987.

[22] A.R. Wieting, M.S. Holden, Experimental Shock-Wave Interference Heating on a Cylinder at Mach 6 and 8, AIAA J. 27 (1989) 1557–1565.

[23] M.J. Wright, et al., Numerical and experimental investigation of double-cone shock interactions, AIAA J. 38 (2000) 2268–2276.

[24] K. Xu, Gas-kinetic schemes for unsteady compressible flow simulations, VKI for Fluid Dynamics Lecture Series 1998-03 (1998), Computational Fluid Dynamics.

[25] K. Xu, A gas-kinetic BGK scheme for the Navier–Stokes equations and its connection with artificial dissipation and Godunov method, J. Comput. Phys. 171 (2001) 289–335.

[26] K. Xu, X.Y. He, Lattice Boltzmann method and gas-kinetic BGK scheme in the lower Mach number viscous flow simulations, J. Comput. Phys. 190 (2003) 100–117.

[27] S. Yamamoto, S. Kano, H. Daiguji, An efficient CFD approach for simulating unsteady hypersonic shock–shock interference flows, Comp. Fluids 27 (1998) 571–580.

[28] S. Yoon, A. Jameson, Lower-upper symmetric Gauss–Seidel method for the Euler and Navier–Stokes equations, AIAA J. 26 (9) (1988) 1025–1026.

[29] X.L. Zhong, Application of essentially nonoscillatory schemes to unsteady hypersonic shock–shock interference heating problems, AIAA J. 32 (1994) 1606–1616.

[30] W.G. Zong, High-order compact schemes and their application to the calculation of complex flows, Ph.D. Thesis, China Aerodynamics Research and Development Center, Mianyang, China, 2000.